Estimation and Modeling of Enceladus Plume Jet Density Using Reaction Wheel Control Data†

Allan Y. Lee,[1] Eric K. Wang,[1] Emily B. Pilinski,[2] Glenn A. Macala,[1] and Antonette Feldman[1]

[1]Jet Propulsion Laboratory, 4800 Oak Grove Drive, Pasadena, CA 91109-8099
California Institute of Technology

[2]University of Colorado, Boulder, Colorado 80309

The Cassini spacecraft was launched on October 15, 1997 by a Titan 4B launch vehicle. After an interplanetary cruise of almost seven years, it arrived at Saturn on June 30, 2004. In 2005, Cassini completed three flybys of Enceladus, a small, icy satellite of Saturn. Observations made during these flybys confirmed the existence of a water vapor plume in the south polar region of Enceladus. Five additional low-altitude flybys of Enceladus were successfully executed in 2008-9 to better characterize these watery plumes. The first of these flybys was the 50-km Enceladus-3 (E3) flyby executed on March 12, 2008. During the E3 flyby, the spacecraft attitude was controlled by a set of three reaction wheels. During the flyby, multiple plume jets imparted disturbance torque on the spacecraft resulting in small but visible attitude control errors. Using the known and unique transfer function between the disturbance torque and the attitude control error, the collected attitude control error telemetry could be used to estimate the disturbance torque. The effectiveness of this methodology is confirmed using the E3 telemetry data. Given good estimates of spacecraft's projected area, center of pressure location, and spacecraft velocity, the time history of the Enceladus plume density is reconstructed accordingly. The 1σ uncertainty of the estimated density is 7.7%. Next, we modeled the density due to each plume jet as a function of both the radial and angular distances of the spacecraft from the plume source. We also conjecture that the total plume density experienced by the spacecraft is the sum of the component plume densities. By comparing the time history of the reconstructed E3 plume density with that predicted by the plume model, values of the plume model parameters are determined. Results obtained are compared with those determined by other Cassini science instruments.

†This paper is dedicated to the memory of Dr. Shuh-Ren Randy Lin who had contributed to the designs of several Enceladus flyby sequences by the Cassini spacecraft.

I. Cassini/Huygens Mission to Saturn and Titan

As the first spacecraft to achieve orbit at Saturn in 2004, Cassini has collected science data throughout its four-year prime mission, and has since been approved for a first and second extended mission through 2017. Major science objectives of the Cassini mission include investigations of the configuration and dynamics of Saturn's magnetosphere, the structure and composition of the rings, the characterization of several of Saturn's icy satellites, and Titan's atmosphere constituent abundance. The radar mapper will perform surface imaging and altimetry during many Titan flybys. Doppler tracking experiments using the Earth and the Cassini spacecraft as separated test masses have also been conducted for gravitational wave searches.

After an interplanetary cruise that lasted almost seven years, on June 30, 2004, Cassini fired one of its two rocket engines for about 96 minutes in order to slow the spacecraft's velocity (by about 626.17 m/s) to allow the spacecraft to be captured by the gravity field of Saturn. This was the most critical engineering event of the entire mission and was executed faultlessly. After the completion of the Saturn Orbit Insertion, Cassini began a complicated suite of orbits about Saturn, designed to optimize science collection over not only Saturn, but also its ice satellites and moons.

The orbital tour of Saturn, includes over fifty flybys of Saturn's largest moon, Titan. Titan is the second largest moon in the Solar System, second only to Jupiter's moon Ganymede. At 5150 kilometers in diameter, Titan is larger than the planet Mercury. Titan orbits Saturn at a distance of 1,222,000 kilometers, taking 15.9 days to complete one revolution. This unique moon is of great interest to scientists because it is the only known moon in the Solar System with a major atmosphere. Titan's atmosphere is 10 times thicker than the Earth's with a thick haze extending up to 200 kilometers above the surface obscuring optical observations of the terrain. Through ongoing Earth-based telescope observations as well as data collected by the Pioneer and Voyager spacecraft, scientists now know that Titan's atmosphere is composed primarily of nitrogen. In fact, over 95% of its atmosphere is composed of nitrogen, while only 5% is composed of methane, cyanide, and other hydrocarbons. While one of the Cassini-Huygens Mission primary objectives was the study of Titan via many close flybys during its four-year tour, the exciting discovery of water geysers emanating from Enceladus drove an extensive redesign of the extended mission orbital tour of Saturn.

II. The Discovery of Watery Geysers From Enceladus

Enceladus is a small, icy satellite of Saturn with a mean radius of 252.3 km. Covered in water ice that reflects sunlight like freshly fallen snow, Enceladus reflects almost 100% of the sunlight that strikes it making it one of the brightest objects in the solar system. Because Enceladus reflects so much sunlight, the surface temperature is extremely cold, about -201°C. Parts of Enceladus show craters no larger than 35 km in diameter, while other areas show regions with no craters indicating major resurfacing events in the geologically recent past. There are fissures, plains, corrugated terrain and other crustal deformations. All of this indicates that the interior of the moon may be liquid today, even though it should have been frozen eons ago.

In 2005, Cassini made several flybys of Enceladus: a 1264-km Enceladus-0 flyby on February 17, 2005, a 500-km Enceladus-1 flyby on March 9, 2005, and a 175-km Enceladus-2 flyby on July 14, 2005. Observations made during these flybys confirmed the existence of a water vapor plume in the south polar region of Enceladus.[1-8] Cassini's Ion and Neutral Mass

Spectrometer (INMS) made measurements of the plume density out to a distance of 4000 km from the surface of Enceladus. The radial and angular distributions of the INMS-based gas density estimates suggest a significant contribution to the plume from a source centered near the South polar cap of Enceladus.[4]

Cassini imaging science instruements[1,7] revealed four prominent linear fractures straddling the South polar region, each separated by about 30 km and spanning 130 km in length. These fractures, informally termed "Tiger stripes," show dark flanks in the near-IR and are anomalously warm. They are identified individually as Alexandria, Cairo, Baghdad, and Damascus. The Tiger stripes are a likely source of tectonic activities and plume generation. From these Tiger stripes, materials are vented from the interior of the moon to hundreds of kilometers above the moon's surface. One estimate of the "height" of these plumes is 300 km from the surface.[2] The formation of these stripes are conjectured in Reference 8. Reference 5 conjectured that the Enceladus plume might be the dominant source of materials in the Saturn's E ring system.

The discovery of watery geysers from Enceladus is an important and unexpected discovery made by Cassini. The Enceladus watery plume is one of the key science investigations of the Cassini Equinox mission (an extension of the Cassini Prime mission, from July 2008 to September 2010). It will also be one of the key science objectives for the Cassini-Equinox-Solstice mission (a second mission extension, from October 2010 to May 2017). Eleven Enceladus flybys are currently planned for the Cassini-Equinox-Solstice mission. Figure 1 depicts the Enceladus plume jets imaged during the Enceladus-8 flyby.

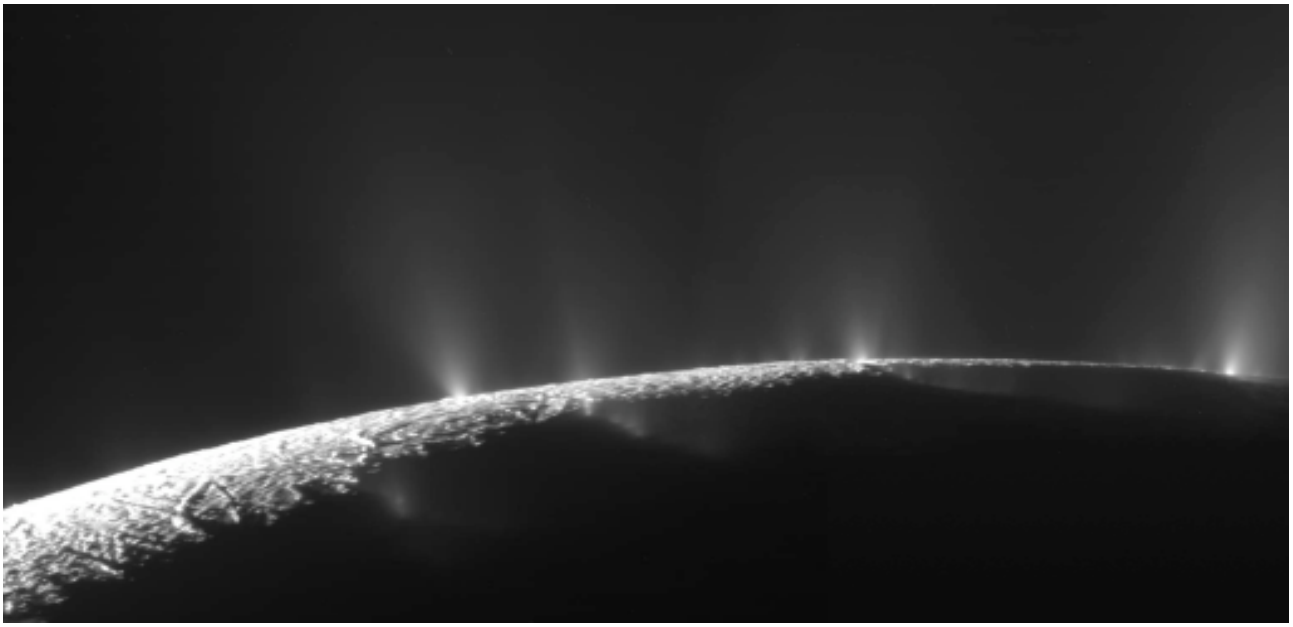

Fig. 1 Enceladus Plume Jets as Imaged by Cassini During the Enceladus-8 Flyby

III. Cassini Spacecraft Configuration[9]

Cassini is perhaps the largest and most sophisticated interplanetary spacecraft humans have ever built and launched. The orbiter is about 6.8 m in height with a "diameter" of 4 meters. The total mass of the spacecraft at launch was approximately 5574 kg, which includes about 3000 kg of bi-propellant (1869 kg of Nitrogen Tetroxide, and 1131 kg of mono-methyl hydrazine), 132 kg of high purity hydrazine, and 2442 kg of "dry" mass (including the 320-kg Huygens Probe and 9 kg of helium mass). Fig. 2 depicts the Cassini spacecraft.

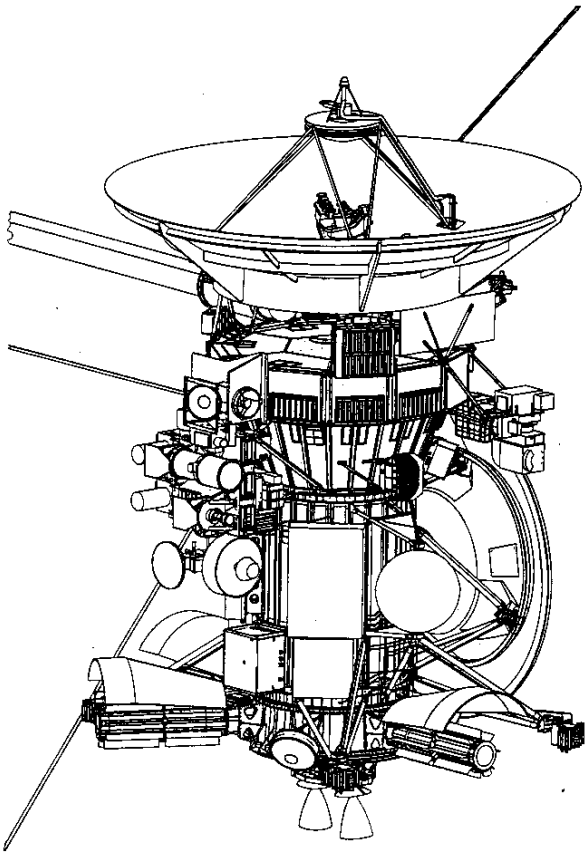

Fig. 2. Cassini Cruise Configuration

The base body of the orbiter is a stack consisting of a lower equipment module, a propellant module, an upper equipment module, and a 4-m High Gain Antenna (HGA). The axis of the stack is the Z-axis of the spacecraft. Attached to the stack are the Remote Sensing Pallet and the Fields and Particles Pallet with their scientific instruments. Until separation, the Huygens probe was attached to the base body with its axis of symmetry pointed parallel to the negative X-axis of the spacecraft. The orbiter's 12-bay electronics bus is part of the upper equipment module. An 11-m magnetometer boom is mounted to the upper equipment module.

The 4-m parabolic HGA and two Low Gain Antennas (LGAs) are the main communication antennas of the spacecraft. An X-band feed is used for both uplink and downlink

communications. For communications, the Attitude and Articulation Control System (AACS) must point the X-band radio-frequency bore-sight of HGA to Earth. At other times, especially while the spacecraft is in the inner Solar System, AACS must point the HGA axis of symmetry to the Sun so that the antenna will shade most of the spacecraft. During certain hazardous Saturn ring-plane crossings, the HGA axis is pointed parallel to the velocity vector of the orbiter (relative to the ring particles) in order to protect most of spacecraft instruments from the incoming energetic ring particles.

During early Cruise, Cassini used a set of eight thrusters to control the spacecraft's attitude. Figure 3 shows the locations of the four thruster pods that are mounted on a structure that is attached to the lower equipment module. On each one of these pods are mounted two primary thrusters and their "backups." Pointing controls about the S/C's X and Y-axis are performed using four Z-facing thrusters. Controls about the Z-axis are performed using four Y-facing thrusters. Cassini's thrusters have rich heritage from the Voyager program.

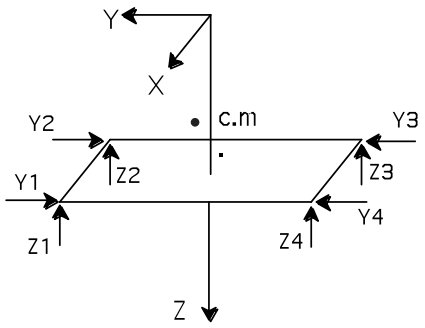

Fig. 3. Cassini Thruster Pod Locations

With reference to Figure 3, we see that to slew about the positive Z-axis of the spacecraft, one must fire both the Y_2 and Y_4 thrusters simultaneously. Thrusts generated by these firings will almost cancel each other, and the ΔV imparted on the spacecraft will be quite small. Similarly, to slew about the negative Z-axis of the spacecraft, one must fire both the Y_1 and Y_3 thrusters simultaneously. Again, the ΔV imparted on the spacecraft will be small. On the other hand, a slew about either the $\pm$X-axis or $\pm$Y-axis will involve firings of the Z-facing thrusters. Since these Z-facing thrusters all point in the same direction, slewing the spacecraft about either the X or Y-axis will generate unwanted ΔV on the spacecraft that must be predicted and incorporated in the spacecraft trajectory design. For this reason, during Tour, the spacecraft was slewed mostly using three prime reaction wheels. The obvious merits of using reaction wheels over thrusters are the absence of unwanted ΔV imparted on the spacecraft and the conservation of hydrazine.

IV. Cassini Spacecraft Reaction Wheel Control System Design

Cassini carries a set of three "strap-down" reaction wheels that are mounted on the lower equipment module. They are oriented "equal distance" from the spacecraft's Z-axis. The first use of the reaction wheel control was on March 16, 2000, several months ahead of the Jupiter science campaign that began on October 1, 2000. A backup reaction wheel assembly (RWA) is mounted on top of an articulatable platform. At launch, the backup reaction wheel is mounted parallel to reaction wheel assembly – 1 (RWA-1). On July 11, 2003, the platform was articulated in order to

align the backup reaction wheel with RWA-3. Figure 4 depicts the orientations of the four RWAs relative to the spacecraft's coordinate frame at launch. Figure 5 (from Ref. 10) is an illustration of the RWA controller (RWAC) design.

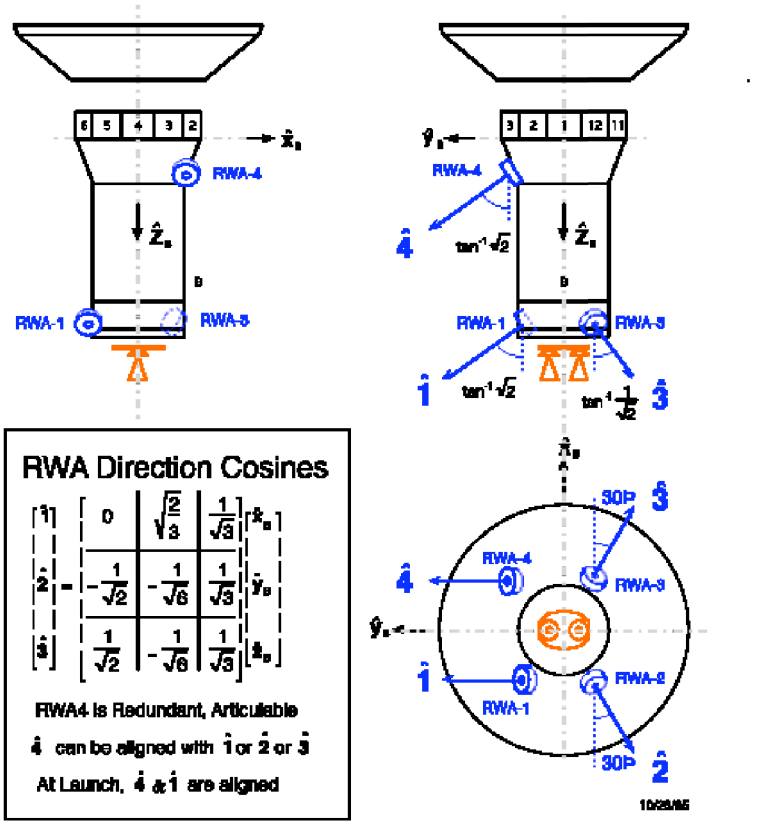

Fig. 4. Cassini Reaction Wheel Locations and Orientations[9,10]

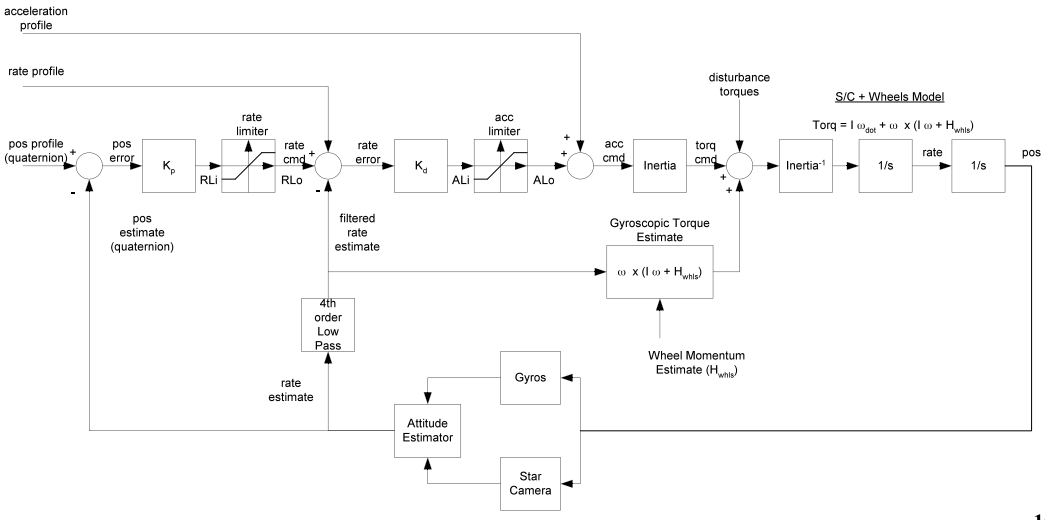

Fig. 5. Block Diagram of the Reaction Wheel-based Attitude Control System[10]

Because the Cassini spacecraft's principle axes are very closely aligned with the spacecraft's mechanical axes, the basic structure of the RWAC is a decoupled, three-axis, Proportional and Derivative (PD) controller. As indicated in Figure 5, the control torque vector is determined using the equation:

$$\text{Control Torque Vector} = I_{SC}d\omega/dt+\omega\times(I_{SC}\omega+H_{RWA}) \quad (1)$$

Here, ω is the spacecraft rate vector (that is expressed in a body-fixed coordinate frame), H_{RWA} represents the total angular momentum vector of the three prime wheels (that is expressed in the same coordinate frame), I_{SC} is the inertia tensor of the vehicle (determined with stationary reaction wheels), and $d\omega/dt$ is the spacecraft's acceleration. The second term in the equation represents the gyroscopic torque vector.

An important design feature that is depicted in Fig. 5 is the uses of the rate and acceleration feed-forward commands. These feed-forward commands generate immediate control action instead of "waiting" for the accumulation of error signals via the feedback loops. As such, the RWAC responds quickly to profiled slew commands. The feed-forward command is generated by the Attitude Commander. It derives these signals using commands sent by the spacecraft control team.

Due to the presence of bearing frictional torque in the reaction wheels, an RWAC with the "PD" control architecture will not be able to drive the spacecraft attitude control error to zero unless an integral term is added to the PD controller. This difficulty was overcome by the addition of a Proportional and Integral (PI) estimator of the reaction wheel frictional torque in the reaction wheel "Hardware Manager." In effect, integral control action is added "locally" to remove any steady-state spacecraft's attitude control errors. The RWAC design has a bandwidth of 0.0299 Hz (ω_n). The gain and phase margins of RWAC are 10 dB and 30°, respectively. Flight performance of the RWAC is described in References 9 and 10.

In response to the commanded attitude $\theta_C(s)$, commanded attitude rate $\omega_C(s)$, commanded attitude acceleration $\alpha_C(s)$, and experiencing an external disturbance torque $T_D(s)$, the spacecraft attitude $\theta(s)$, is given by:

$$\theta(s)= G_\theta(s)\theta_C(s)+G_\omega(s)\omega_C(s)+G_\alpha(s)\alpha_C(s)+G_T(s)[T_D(s)+ T_{Gyroscopic}(s)] \quad (2)$$

In this expression, "s" is the Laplace operator, and various G(s) terms represent transfer functions from the command signals (or disturbance torque) to the spacecraft attitude. Without loss of generality, consider a special case when the reaction wheels are used to maintain a constant spacecraft attitude during an Enceladus flyby, therefore $\theta_C = \omega_C = \alpha_C = 0$. Since the nominal rate vector of the spacecraft is zero, the gyroscopic term in Eq. (2) is also zero. From Ref. 10, the transfer function between the disturbance torque $T_D(s)$ and the attitude control error $e_\theta(s)$ is given by:

$$\frac{e_\theta(s)}{T_D(s)} = -\frac{(s^2 + 2\xi\omega s + \omega^2)^2/I_{SC}}{\text{Den}(s)} \quad (3)$$

The denominator in Eq. (3) is given by the following expression:

$$\begin{aligned}\text{Den(s)} &= s^6 + 4\xi\omega s^5 + (4\omega^2\xi^2 + 2\omega^2 + 4K_PK_D)s^4 + \\ &(4\omega^3\xi + 4K_PK_D\omega\xi)s^3 + (\omega^4 + 4K_PK_D\omega^2\xi^2 + 2K_PK_D\omega^2)s^2 + \\ &(K_D\omega^4 + 4K_PK_D\omega^3\xi)s + K_PK_D\omega^4\end{aligned} \tag{4}$$

In Eq. (3) and (4), the natural frequency (ω) and damping coefficient (ξ) of the 4th order low-pass filter are 2.34048 rad/s and 0.4000, respectively. The proportional (K_P) and derivative (K_D) gains of the RWA controller are given by: $K_P = \omega_n/(2\xi_n)$, and $K_D = 2\omega_n\xi_n$. Here, $\omega_n = 2\pi\times0.0299$ rad/s (RWAC bandwidth), and $\xi_n = 0.4138$ (dimensionless).

Since the bandwidth of the RWA controller is more than an order of magnitude lower than the center frequency of the low-pass filter, a low-order approximation of Eq. (3) could be derived by ignoring the 4th order low-pass filter depicted in Fig. 5:

$$\begin{aligned}\frac{e_\theta(s)}{T_D(s)} &= -\frac{1/I_{SC}}{s^2 + K_Ds + K_PK_D} = -\frac{1/I_{SC}}{s^2 + 2\xi_n\omega_n s + \omega_n^2} \\ &= -\frac{0.0002747}{s^2 + 0.15548s + 0.03529}\end{aligned} \tag{5}$$

From this equation, one can estimate the disturbance torque using the following equation:

$$T_D(t) \approx -3640.4\{\ddot{e}_\theta(t) + 0.15548\dot{e}_\theta(t) + 0.03529e_\theta(t)\} \text{ Nm} \tag{6}$$

In Eq. (6), the attitude control error $e_\theta(t)$, in radians, is given by the per-axis attitude control errors (Telemetry channels that correspond to the per-axis attitude control errors, X, Y, and Z-axis, are A-1180 to A-1182, respectively, given in mrads).[9] The term $\dot{e}_\theta(t)$ in Eq. (6), in rad/s, is computed using both the attitude control errors and the attitude rate control errors (Telemetry channels that correspond to the per-axis attitude rate control errors, X, Y, and Z-axis, are A-1183 to A-1185, respectively, given in rad/s). In Eq. (7) below, 6th order polynomials are used to generate "smoothed" versions of this telemetry. For example, the Z-axis attitude control error telemetry is approximated by

$$A_{1182}(t) = \sum_{i=0}^{6} k_i t^i \tag{7}$$

The "smoothed" telemetry data are then used to estimate $e_\theta(t)$, $\dot{e}_\theta(t)$, and $\ddot{e}_\theta(t)$ via:

$$\begin{aligned}e_\theta &= +A_{1182} \\ \dot{e}_\theta &= -K_PA_{1182} + A_{1185} \\ \ddot{e}_\theta &= 2^{\text{nd}} \text{ derivative of } A_{1182}\end{aligned} \tag{8}$$

Another reduced-order transfer function of Eq. (3) could be derived via an examination of the relative magnitudes of the Hankel singular values of the 6th order transfer function (cf. Eq. (3)). Hankel singular values measure the contribution of each state to the input/output behavior of the system. States with small Hankel singular values indicate that they have limited contribution to the input-output mapping of the transfer function and are candidates for "deletion". In this study,

we use the *Model Reduction Toolbox* of MATLAB© to perform the needed computations. Four system "states" are deleted and the 6th order transfer function becomes a 2nd order transfer function:

$$\frac{e_\theta(s)}{T_D(s)} = -\frac{0.0003091}{s^2 + 0.1753s + 0.03977}$$
$$T_D^Z(t) \approx -\frac{1}{0.0003091}\{\ddot{e}_\theta(t) + 0.1753\dot{e}_\theta(t) + 0.03977 e_\theta(t)\} \text{ Nm} \quad (9)$$

A comparison of the frequency responses of transfer functions represented by Eqs. (3) and (9) is depicted in Fig. 6. Clearly, the second-order transfer function Eq. (9)) approximates the full-order transfer function very well. It is used in our study. Finally, a vector-matrix version of Eq. (5) is given below:

$$\begin{bmatrix} T_D^X(t) \\ T_D^Y(t) \\ T_D^Z(t) \end{bmatrix} = -\begin{bmatrix} I_{XX} & I_{XY} & I_{XZ} \\ I_{XY} & I_{YY} & I_{YZ} \\ I_{XZ} & I_{YZ} & I_{ZZ} \end{bmatrix} \begin{bmatrix} \ddot{e}_\theta^X(t) + 2\xi_n\omega_n\dot{e}_\theta^X(t) + \omega_n^2 e_\theta^X(t) \\ \ddot{e}_\theta^Y(t) + 2\xi_n\omega_n\dot{e}_\theta^Y(t) + \omega_n^2 e_\theta^Y(t) \\ \ddot{e}_\theta^Z(t) + 2\xi_n\omega_n\dot{e}_\theta^Z(t) + \omega_n^2 e_\theta^Z(t) \end{bmatrix} \quad (10)$$

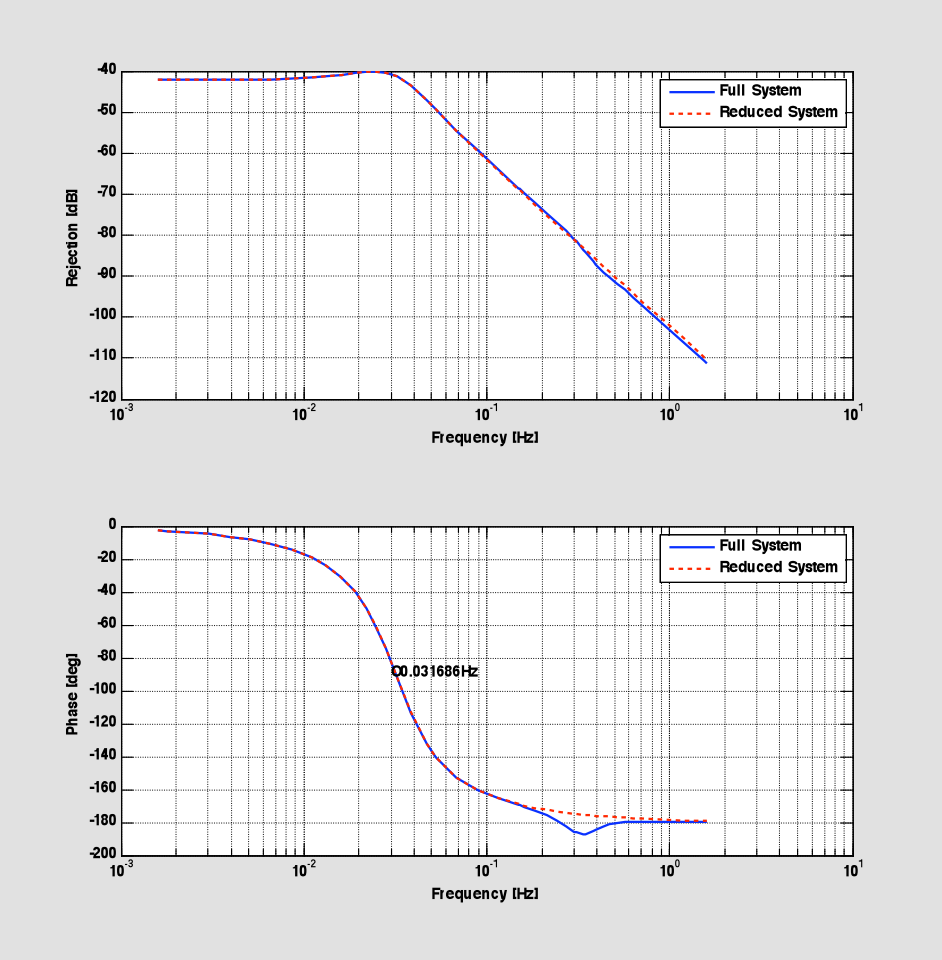

Fig. 6 Frequency Responses of the Full-order and Reduced-order Models

V. Observed Attitude Control Errors During Enceladus-3 Flyby

The attitude of the Cassini spacecraft could be controlled using either a set of eight thrusters or a set of three reaction wheels. Thrusters are used to control the spacecraft attitude during low-altitude Titan and low-altitude Enceladus flybys. During these flybys, Cassini will experience significant atmospheric or plume torque, and only thrusters have the control authority to guarantee spacecraft safety. Because the predicted magnitudes of plume torque imparted on the spacecraft during selected Enceladus flybys are within the control authority of the wheels, some Enceladus flybys were executed using reaction wheels (cf. Table 1). During an Enceladus flyby on thruster control, the watery plume will impart torque on Cassini. As such, thrusters must be fired to maintain the commanded spacecraft flyby attitude. Thrusters' on-time telemetry collected could be used to estimate the magnitude of the imparted torque, and indirectly the density of the Enceladus plume. Similarly, if the spacecraft is controlled by reaction wheels during the flyby, changes in the reaction wheel rates could also be used to estimate the plume torque imparted on the spacecraft. This paper explores an alternative way to estimate the imparted torque using telemetry data of both attitude control and attitude rate control errors.

Table 1. Descriptive Statistics of Targeted Enceladus Flybys on RWA Control

Flyby Designation	Distance at Closest Approach	Location of Closest Approach	Enceladus-relative flyby velocity	Date of Flyby	Telemetry described in Appendix
Enceladus-3	50 km	20^{o} S, 135^{o} W	14.4 km/s	March 12, 2008	B and Section V
Enceladus-4	50 km	28^{o} S, 98^{o} W	17.7 km/s	August 11, 2008	A
Enceladus-9	99 km	89^{o} S, 147^{o} W	6.51 km/s	April 28, 2010	C

Attitude control telemetry data collected from several past RWA-based Enceladus flybys (Enceladus-3, Enceladus-4, and Enceladus-9) revealed the presence of attitude control error transients when the spacecraft was close to the surface of Enceladus. Fig. 7 and Fig. 8 depict the time histories of the three per-axis attitude control errors (A-1180 to A-1182) and attitude rate control errors (A-1183 to A-1185) collected from the Enceladus-3 flyby, respectively. Obviously, for this particular flyby, most of the disturbance torque experienced by the spacecraft is about the spacecraft's Z-axis. As such, the Z-axis attitude control error and attitude rate control error are significantly larger than their counterparts about both the X and Y-axis. These Z-axis telemetry data could be used to estimate the Z-axis disturbance torque.

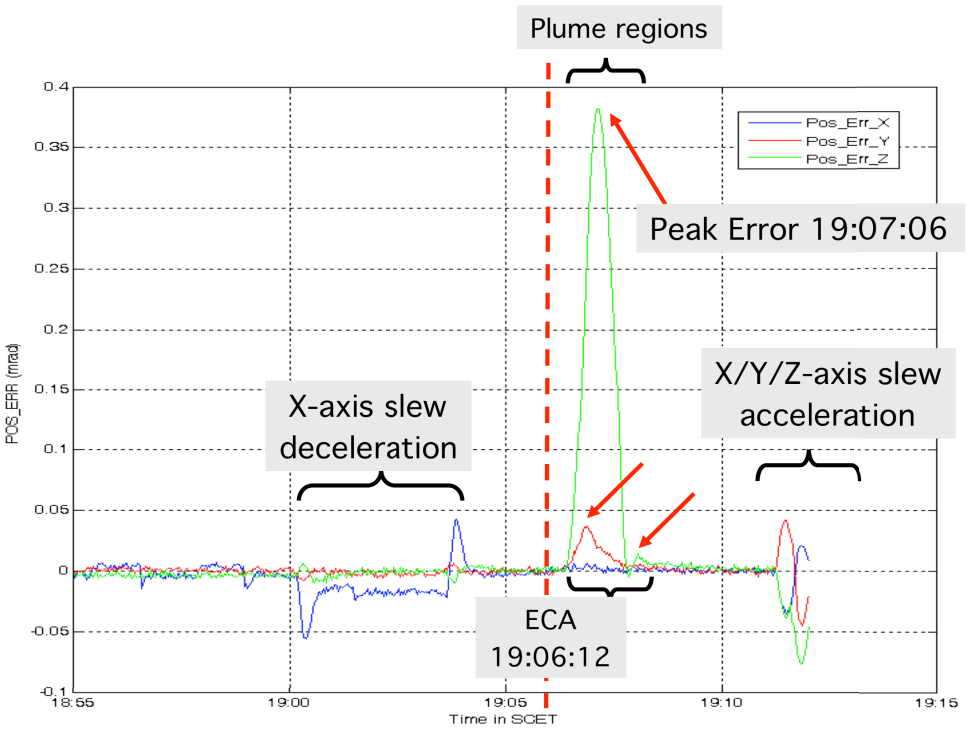

Fig. 7 Per-axis Attitude Control Errors of Enceladus-3 Flyby

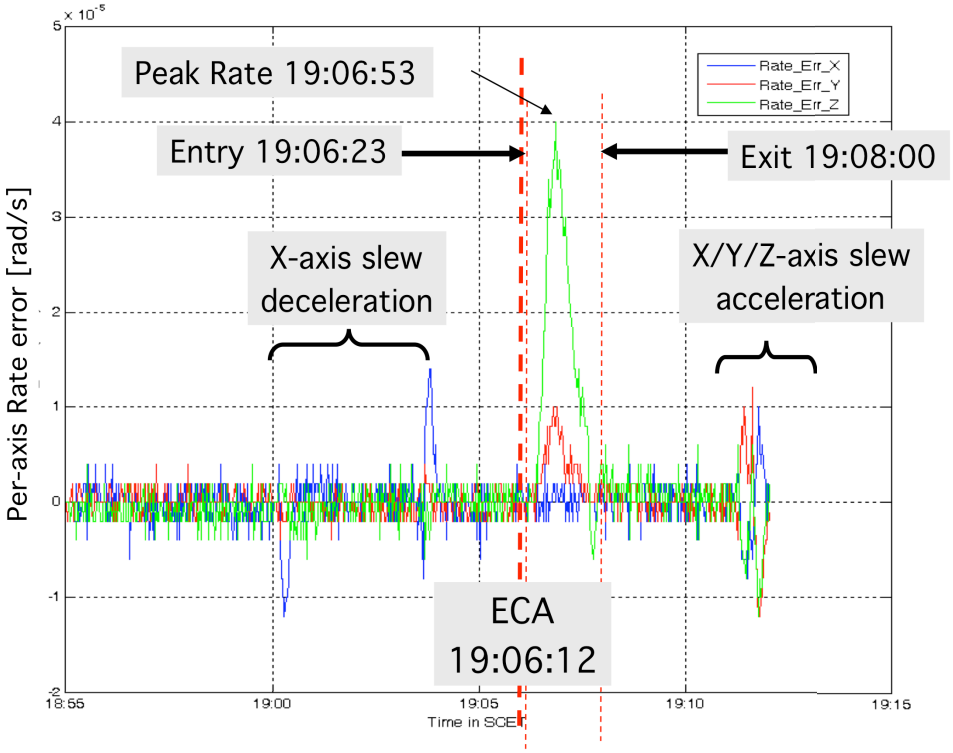

Fig. 8 Per-axis Attitude Rate Control Errors of Enceladus-3 Flyby

VI. Reconstructed Disturbance Torque Experienced by Cassini during the E3 Flyby

The inertia properties of the spacecraft, at the time of Enceladus-3 flyby is given by:

$$I_{SC} = \begin{bmatrix} 6957.6 & -124.8 & -38.7 \\ -124.8 & 5751.5 & 133.0 \\ -38.7 & 133.0 & 3640.4 \end{bmatrix} \quad \text{kg-m}^2 \tag{11}$$

Note that in the 3rd row of the inertia matrix, both element (3,1) and (3,2) are less than 3.6% of the (3,3) element. Moreover, since both $e_X(t)$ and $e_Y(t)$ are very small when compared with $e_Z(t)$ (see Figs. 7 and 8), the Z-axis plume torque imparted on Cassini during Enceladus-3 could be computed using Eq. (9). The resultant time history of the Z-axis plume torque is depicted in Fig. 9. Note that the peak torque magnitude is -0.0204 Nm, and it occurred at time ≈ ECA+34 s. The torque imparted on the spacecraft during the flyby caused the spacecraft's Z-axis attitude rate control error to peak at ECA+41 s (cf. Fig. 8). Some time thereafter, the spacecraft's Z-axis attitude control error peaked at ECA+54 s (cf. Fig. 7). Knowing that the peak torque occurred at ECA+34 s (see Fig. 9), and the actual altitude of ECA was 47.9 (instead of 50) km,[24] we can compute the spacecraft's altitude at the time the peak torque occurred. It is about 322.3 km. Its location relative to the Enceladus plume is given in Fig. 13.

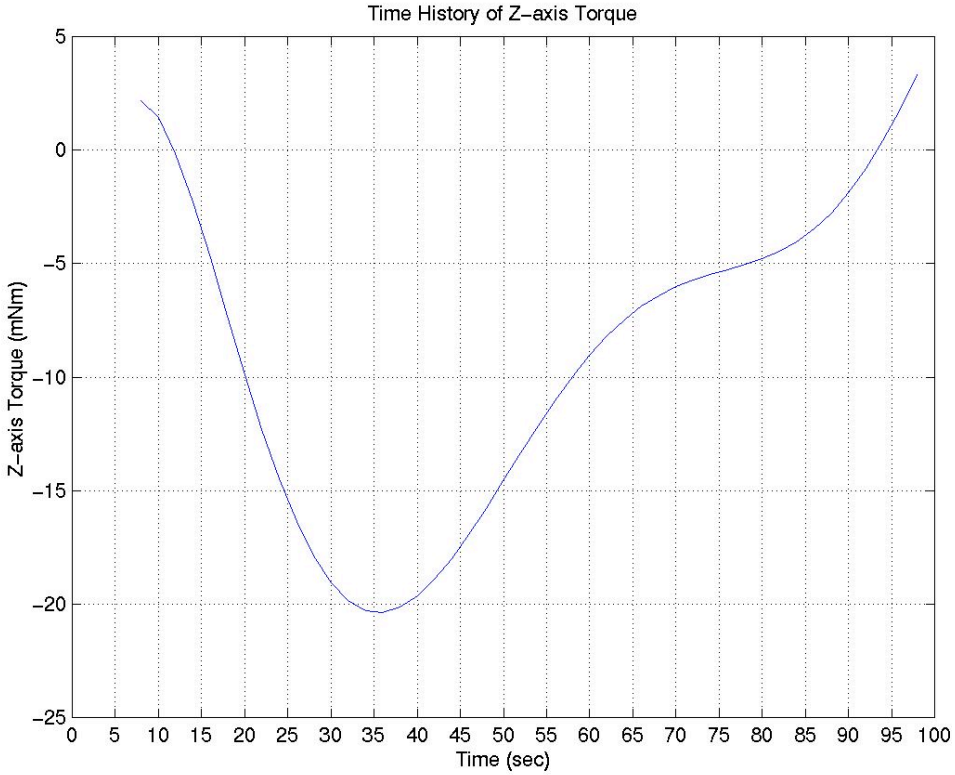

Fig. 9 Reconstructed Z-axis Torque Imparted on the Spacecraft during Enceladus-3 Flyby (Enceladus Closest Approach is at Time = 0)

The time rates of change of the per-axis accumulated angular momenta could also be used to reconstruct the magnitudes of the per-axis disturbance torque imparted on the spacecraft. In order to maintain the quiescent inertial attitude of the spacecraft, the three RWAs must "absorb" the angular momenta imparted on Cassini due to the (time-varying) plume-induced torque. As a result, the RWA spin rates changed as the spacecraft passed through the plume cloud. The total angular momentum of the spacecraft could be computed using knowledge of the RWAs' inertia properties, the S/C inertia properties, and the telemetry data of the S/C's rates and RWA spin rates. The total angular momentum vector of the spacecraft, expressed in the spacecraft body frame, has two components:

$$\vec{H}_{Total} = \vec{H}_{SC} + \vec{H}_{RWA} \tag{12}$$

where the component due to the spacecraft rate is

$$\vec{H}_{SC} = I_{SC}\vec{\omega} \tag{13}$$

and

$$\vec{\omega} = [\omega_x, \omega_y, \omega_z]^T \tag{14}$$

To determine the angular momentum of the RWAs, we first define

$$\vec{\rho} = [\rho_1, \rho_2, \rho_4]^T \tag{15}$$

where ρ_i (i=1,2, and 4) is the spin rate of the i^{th} RWA about its spin axis. To find $\vec{H}_{RWA}$, we simply multiply $\vec{\rho}$ first by the inertia matrix for the RWAs, and then multiply by the transformation matrix T.

$$\vec{H}_{RWA} = TI_{RWA}\vec{\rho} \tag{16}$$

The 3×3 RWA-to-S/C coordinate transformation matrix T is given in Fig. 4, and the 3×3 diagonal inertia matrix of the reaction wheels $I_{RWA} = \text{diag}(0.16138, 0.15947, 0.16138)^T$ kg-m^2. The computed time histories of the Z-axis angular momentum is given in Fig. 10. Note that both the per-axis spacecraft rates and the reaction wheel spin rates are available at a telemetry frequency of 0.25 Hz.

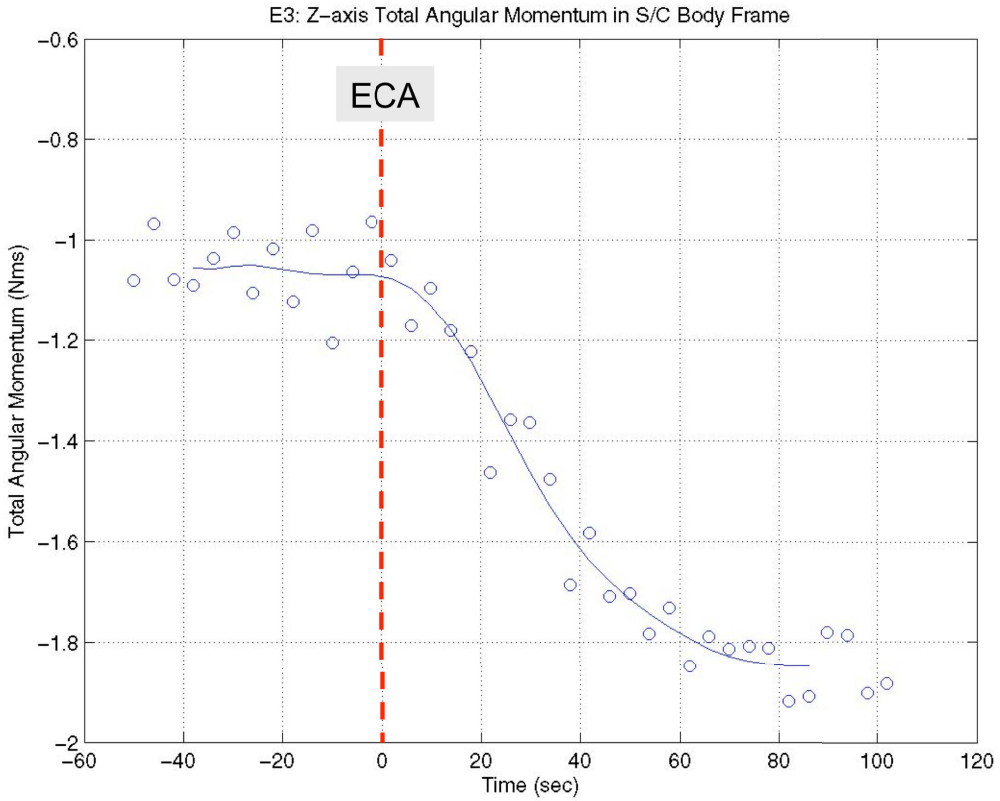

Fig. 10 Computed Z-axis Angular Momentum of Cassini During Enceladus-3 Flyby

The time rates of change of the per-axis angular momenta are the per-axis plume torque imparted on Cassini. For the E3 scenario, only the slope of the Z-axis angular momentum is significant. The slope of the Z-axis angular momentum (as depicted in Fig. 10) is computed numerically. To generate the result given in Fig. 11, we first approximate the Z-axis angular momentum by a 12^{th} order polynomial

$$H^{Z}_{Total}(t) = \sum_{i=0}^{12} p_i t^i \tag{17}$$

and the external torque imparted on the spacecraft is given by

$$T^{Z}(t) = \sum_{i=1}^{12} i p_i t^{i-1} . \tag{18}$$

The peak torques depicted in Fig. 11 is about -0.019 Nm. It occurred near ECA+26 s. The peak torque computed using the "time rate of change of angular momentum" approach agrees quite well with that computed using the "transfer function" approach proposed in this paper (-0.0204 Nm). This comparison is used to estimate the error associated with disturbance torque estimated by the proposed "transfer function" approach. The 1σ estimation uncertainty is judged to be 5%.

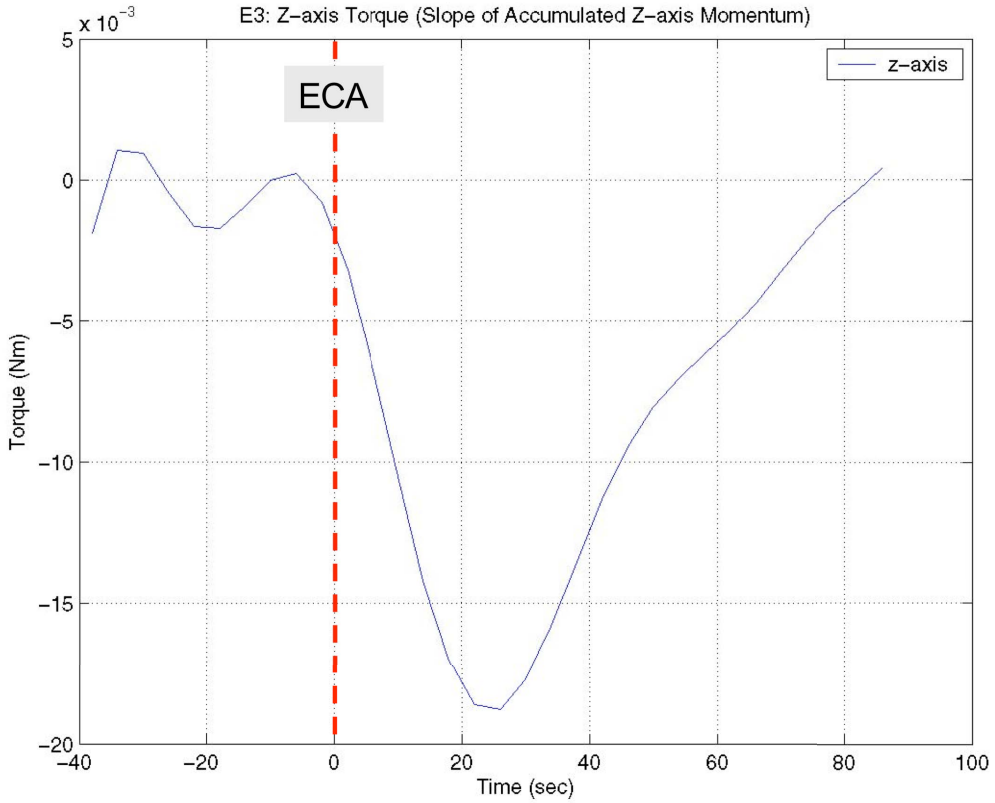

Fig. 11 Computed Z-axis Plume Torque Imparted on Cassini During Enceladus-3 Flyby

Another "disturbance" torque imparted on the spacecraft during an Enceladus flyby is the gravity gradient torque. The magnitude of gravity gradient torque is a function of both spacecraft attitude and its distance from Enceladus. With a worst-case spacecraft attitude, this torque could be estimated using the following expression

$$T_{Gravity-Gradient} = \frac{3}{2}\mu_{Enceladus}\frac{(I_{Max} - I_{Min})}{(R_{Enceladus} + h)^3} \tag{19}$$

Here, $\mu_{Enceladus}$ is the product of the universal gravitational constant and the mass of Enceladus ($\approx$7.207$\pm$0.011 km^3/s^2),[11] $R_{Enceladus}$ is the effective radius of Enceladus ($\approx$ 252.3$\pm$0.2 km),[1,11] h is the spacecraft's Enceladus-relative altitude at the time the torque peaked (322.3 km for the Enceladus-3 flyby), and I_{Max} and I_{Min} are the maximum and minimum moments of inertia of the spacecraft, respectively (cf. Eq. (11)). The *worst-case* magnitude of $T_{Gravity-Gradient}$ is about 190 μNm which is less than 1% of the estimated Z-axis peak torque.

From Ref. 9, the estimated magnitude of the solar radiation torque imparted on Cassini is bounded by 2 μNm, and the radiation torque imparted on the spacecraft due to the Cassini power generators is bounded by 1.83 μNm. These disturbance torques are also very small. Magnetic torque acting on the spacecraft results from the interaction of the spacecraft's residual magnetic field and the magnetic field of Saturn at Enceladus. The magnetic disturbance torque, $T_{Magnetic}$, could be estimated using the following expression

$$T_{Magnetic} = M_{arm} \times B_{Enceladus} \tag{20}$$

Here, M_{arm} is the spacecraft magnetic moment arm, estimated to be 1.4 Amp-m^2, and $B_{Enceladus}$ is the magnetic flux density of Saturn at Enceladus. Enceladus is located in the inner magnetosphere of Saturn at a radial distance of 3.94 R_S (1 R_S = 60,268 km). The magnetic field strength in this region is ≈ 320 nT (nano-Telsa, Tesla ∈ kg-s^{-2}-A^{-1}).[18] It is also estimated that the Enceladus plume has at most a 10% impact on the magnetic flux density.[19] Accordingly, the estimated worst-case magnitude of $T_{Magnetic}$ is 0.5 μNm. Since the gravity gradient torque, solar radiation torque, radiation torque due to power generators, and magnetic torque are all insignificant, the estimated torque imparted on the spacecraft is due solely to the watery plume.

VII. Reconstructed Density of Enceladus Plume Jets

The Enceladus plume density is related to the torque imparted on the spacecraft by the following approximate relation:[9,12-14]

$$\vec{T}_{Plume}(t) \approx \frac{1}{2} C_D \rho_{Plume}(t) V(t)^2 A_{Projected}(t) \;\; \vec{u}_V(t) \times [\vec{r}_{CP}(t) - \vec{r}_{CM}] \tag{21}$$

In this equation, $T_{Plume}(t)$ is the torque imparted on the spacecraft that was estimated using the approach described above. $\rho_{Plume}(t)$ is the time history of the Enceladus plume density, in kg/m^3, and is the "unknown" quantity. The spacecraft velocity relative to Enceladus is denoted by V(t) (in m/s), and is estimated by the Cassini Navigation team for all Enceladus flybys. The unit vector of the S/C's velocity vector expressed in the S/C's coordinate frame is $\vec{u}_v(t)$. The projected area of the spacecraft is $A_{Projected}$ (in m^2). The displacement vectors, from the origin of the spacecraft coordinate frame to the spacecraft's center of mass and center of pressure (in meters) are denoted by $\vec{r}_{CM}(t)$ and $\vec{r}_{CP}(t)$, respectively. These vectors and the projected area were estimated by a ground software tool. Finally, C_D, the drag coefficient associated with the free molecular flow of Enceladus' plume constituents past the body of the Cassini spacecraft, was known from past research: $C_D \approx 2.1 \pm 0.1$.[9] For Enceladus-3, at the time of closest approach, V = 14.41 km/s, $A_{projected}$ = 18.401 m^2, and the Z-axis moment arm of the r_{CP}-r_{CM} vector = 0.853 m. Accordingly:

$$\vec{T}_{Plume}(t) = 3.422 \times 10^{+9} \rho_{Plume}(t) \tag{22}$$

Since the peak torque is 0.0204 Nm, the peak density of the Enceladus plume is 5.96×10^{-12} kg/m^3. The peak density that is estimated using the "angular momentum" approach is 5.6×10^{-12} kg/m^3. The combined 1σ estimation uncertainty of knowledge errors of C_D, V, $A_{projected}$, $\vec{r}_{CM}$ and $\vec{r}_{CP}$ in Eq. (21) is 5.9%.[12] The overall 1σ uncertainty of the estimated density is RSS(5,5.9) = 7.73%.

VIII. Modeling of Enceladus' Plume Jet Density

The geometry of the Enceladus-3 flyby is depicted in Figs. 12 and 13. The thick red line in Fig. 12 depicts Cassini's flyby trajectory projected onto a plane that is perpendicular to the Enceladus's axis of rotation. The trajectory passed almost exactly over the Cairo source VIII and then the Damascus source II. The trajectory was also very close to Alexandria source IV. Potentially, plumes from these sources had the largest impacts on Cassini. The locations of these plume sources are tabulated in Table 2.

Table 2
Locations of Three Plume Sources that Impacted Cassini During the Enceladus-3 Flyby

Plume Sources	Alexandria	Cairo	Damascus
South latitude (γ_{LAT})*, deg	72.9	82.1	79.4
West longitude (γ_{LON})*, deg	148.7	115.5	315.5
$\Delta=R_E\times\cos(\gamma_{LAT})\times\lvert\gamma_{LON}-135\rvert/57.3^{\#}$, km	17.8	11.8	0.40
Colatitudes $\delta = 90-\gamma_{LAT}$, deg^{+}	+17.1	+7.9	-10.6

*From Reference 7.
$^{\#}$The longitude of the Enceladus-3 trajectory is 135°. See also Figure 12.
$^{+}$With reference to Fig. B1, δ is defined positive in the counter-clockwise direction.

Fig. 13 is a projected view of the Enceladus-3 flyby on a plane formed by the spacecraft trajectory and the axis of rotation of Enceladus. It is drawn to scale. In this figure, "A", "C", and "D" denote the locations of the plume sources, Alexandria, Cairo, and Damascus, respectively (see also Fig. 12). These plume sources are drawn using the latitudes presented in Table 2. Three points on the spacecraft trajectory are labeled "P", "Q", and "R". Point "P" denotes the time (ECA+8 s) at which the Cassni reaction wheel control system first detected and responded to disturbance torque due to the plume jets. After point "R" (ECA+112 s), the reaction wheel control system no longer detected any disturbance torque. Point "Q" (ECA+34 s) is the estimated time at which the detected disturbance torque peaked. The locations of "P", "Q", and "R" are drawn using the timing data depicted in Figs. 7 and 9. Note that "Q" is located very close to the Cairo plume axis and CQ is about 322 km.

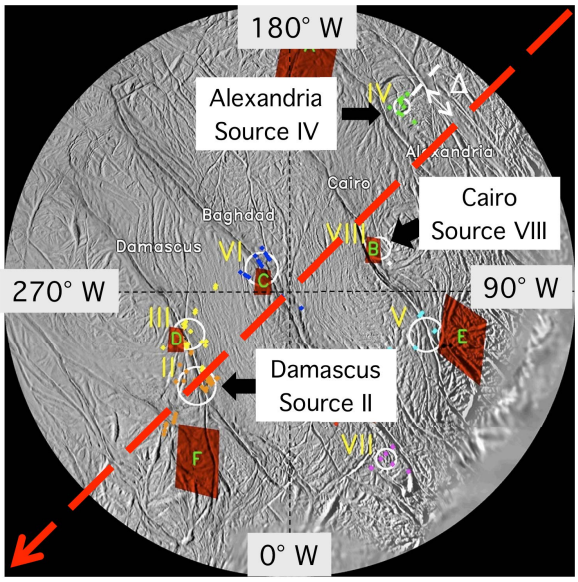

Fig. 12 Enceladus-3 Flyby Trajectory Projected on the Equatorial Plane of Enceladus[20] (The flyby trajectory is depicted by the thick red arrow. The estimated distances Δ's are given in Table 2)

One of the key Cassini science instruments, Ion and Neutral Mass Spectrometer (INMS),[15,16] determines the chemical, elemental, and isotopic composition of the gaseous and volatile components of neutral particles and the low-energy ions in Titan's atmosphere and ionosphere, Saturn's magnetosphere, and the ring environment. With the discovery of watery jets from Enceladus, the INMS has also been used to estimate the Enceladus plume density. Measurements made by the Cassini INMS on the density and structure of Enceladus' south polar plume during the E3 and E5 flybys are reported in Ref. 17. For the E3 flyby, INMS first detected H_2O signal at time ≈ ECA+20 s and the measured signal peaked at ECA+50 s. The magnitude of the peak signal is more than an order of magnitude larger than the "initial" signal. In Ref. 17, the authors attributed the sharp rise in H_2O signal to the fact that at ECA+50 s, Cassini entered the active region of the Damascus plume jet.

If the disturbance torque at "P" (ECA+8 s) came from the first plume jet encountered by Cassini, Alexandria, we noted the angle between the Alexandria plume axis and AP is 82.6°. As such, this observation does not support the conjecture that the plume width of the Alexandria jet is only ±20°.[17] While the influence of the plume jets likely diminishes with the angular distance from the axis of the plume jet, the angular spreads of these jets might be significantly larger than ±20°. In Fig. 13 we note that "R" is located inside the spheres of influence of both the Cairo and Damascus jets, even if one assumed that the plume angular width is only ±20°. At "R" (ECA+112 s), the spacecraft was at distances of 1,400 and 1,390 km from Cairo and Damascus, respectively. Since "R" is the last time the reaction wheel control system detected disturbance torque, our data support the conjecture that the radial extent of the Cairo and Damascus plume jets ended at a distance of approximately 1,300 - 1,400 km (which is about 5.53 Enceladus radii) from the plume sources.

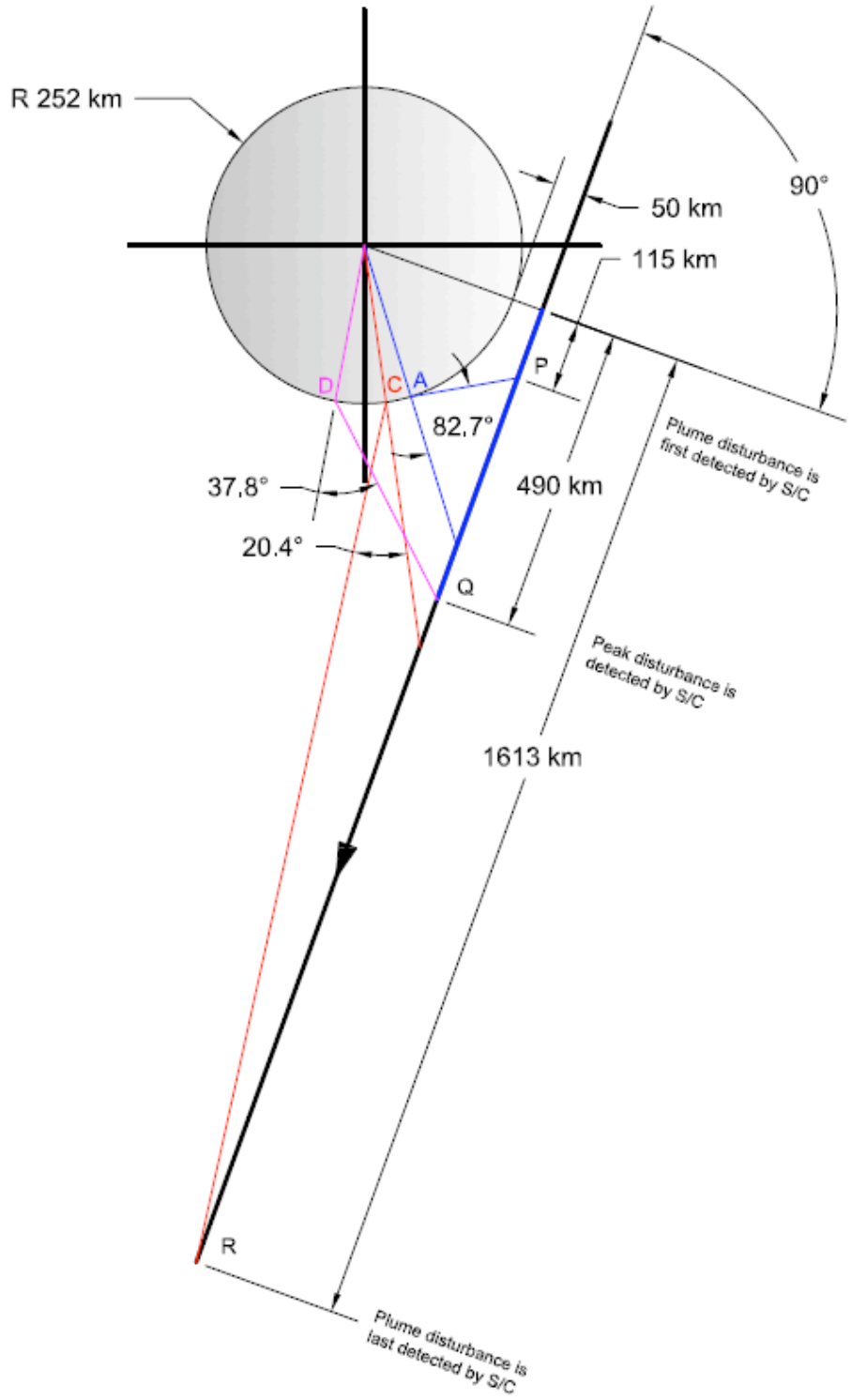

Fig. 13 Projected View of the Enceladus-3 Flyby
(View formed by the trajectory and the Enceladus's axis of rotation. Drawn to scale)

As depicted in Fig. B1 (in Appendix B), the radial distance of the spacecraft from the plume center (on the surface of Enceladus) is denoted by "r(t)". The angular distance, "θ(t)", is the angle between the "r" vector and the axis of symmetry of the corresponding plume jet. If time, t, is measured from the time of Enceladus closest approach, one can compute r(t) and θ(t), for each one of the three plume sources, using the following relations:

$$\begin{aligned}
&\text{For i = Alexandria, Cairo, and Damascus,}\\
&p_i(t) = (R_E + h_{ECA})\cos\alpha - Vt\sin\alpha - R_E\sin\delta_i\\
&q_i(t) = (R_E + h_{ECA})\sin\alpha + Vt\cos\alpha - R_E\cos\delta_i\\
&r_i(t) = \sqrt{p_i(t)^2 + q_i(t)^2 + \Delta_i^2}\\
&\theta_i(t) = \left|\tan^{-1}\left(\frac{p_i(t)}{q_i(t)}\right) - \delta_i\right|
\end{aligned} \tag{23}$$

Here, R_E = Radius of Enceladus = 252.3 km, h_{ECA} = altitude of Enceladus-3 closest approach = 47.9 km,[24] α = South latitude of the Enceladus-3 closest approach = 20°, and V = Velocity of Cassini relative to Enceladus = 14.41 km/s. The colatitudes δ and Δ, and their magnitudes for the plume sources are given in Table 2. In this study, we model the plume density (due to each source) as a function of both the radial and angular distances (r,θ) of the spacecraft from the plume. For simplicity, only two "free" parameters are retained in each plume model (cf. Eq. (25)). We also conjecture that the total plume density experienced by the spacecraft is the sum of the component plume densities. By comparing the time history of the reconstructed E3 plume density with that predicted by the plume model, values of the "free" model parameters could be determined.

In Ref. 21, the structure of the Enceladus plume density is modeled using the following relation

$$n_n(R,\Theta) = n_0\left[\frac{R_E}{R}\right]^2 \exp\left[-\left(\frac{\Theta}{H_\Theta}\right)^2\right]\exp\left[-\frac{R - R_E}{H_d}\right] \tag{24}$$

where n_0 is the plume density at the plume site on Enceladus's surface, R the radial distance from the center of Enceladus, Θ is the angular distance from the plume center, H_Θ is the angular width of the plume, and H_d is a depletion length scale. Other details of this plume density model are given in Ref. 21. In our study, a similar but simplified model is used.

$$\rho^i(r_i,\theta_i) = K_\rho^i\left[\frac{R_E}{r_i}\right]^{\frac{3}{2}} \exp\left[-\frac{\theta_i}{K_\theta^i}\right] \quad \text{(for i = Alexandria, Cairo, and Damascus)} \tag{25}$$

Note that, for simplicity, the two terms that are used in Eq. (24) to describe the dependency of density on the radial distance R have been "combined" in Eq. (25). Note also that the radial distance from the plume source r_i (in km) is used in Eq. (25) instead of the radial distance R from the center of Enceladus. To avoid the singularity at r_i = 0 km, we will restrict the use of Eq. (25) to $1{,}400 \geq r_i \geq 50$ km. A relation $\rho \in 1/r$ was used in Ref. 25 to model the dependency of the intensity of the dust jets from Comet 19P/Borrelly with radial distance. A relation $\rho \in 1/r^2$ was

used in Ref. 17 to model the dependency of the Enceladus plume jet density with radial distance from the surface of Enceladus. In this work, a relation $\rho \in 1/r^{1.5}$ is used instead because it will provide a better fit between the reconstructed density and the model density. The magnitude of radial distance, θ_i, is by definition positive with units of radians. The units of K_ρ^i and K_θ^i (i = Alexandria, Cairo, and Damascus) are kg/m^3 and radians, respectively.

In our study, we assume that the combined plume density during the Enceladus-3 flyby is given by

$$\rho_{\text{Model}}^{\text{E3}}(t) = \sum_{i=\text{Alexandria, Cairo}}^{\text{Damascus}} \rho^i(r_i(t), \theta_i(t)) \tag{26}$$

The six "free" plume density model parameters, K_ρ^i and K_θ^i (i = Alexandria, Cairo, and Damascus), are to be selected to minimize the following modeling error between the reconstructed density $\rho_{\text{Reconstructed}}^{\text{E3}}(t)$ and the modeled density $\rho_{\text{Model}}^{\text{E3}}(t)$ or

$$\text{Model Error} = \sqrt{\frac{1}{t_{\text{Exit}} - t_{\text{Entry}}} \int_{t=\text{Entry}}^{t=\text{Exit}} [\rho_{\text{Model}}^{\text{E3}}(t) - \rho_{\text{Reconstructed}}^{\text{E3}}(t)]^2 dt} \tag{27}$$

These parameters could be determined using the simplex method described in Ref. 22. The effectiveness of this method has been proven in many applications.[23] Values of model parameters that minimize the model error are given in Table 3. Note that the value of the angular widths of the plumes K_θ^i (i = Alexandria, Cairo, and Damascus) that achieved a good match between the model and reconstructed plume density is about 20°. This value is close to the plumes' angular widths mentioned in Ref. 17. Ref. 21 provided evidence for temporal variation of Enceladus' plume jets. Since these parameter values are estimated using E3 data, they might not be applicable for jets encountered in other Enceladus flybys.

Table 3 Selected Values of Enceladus Plume Density Model Parameters (for E3 only)

Plume Sources	Alexandria	Cairo	Damascus
K_ρ^i (kg/m^3)	0.55×10^{-12}	10.3×10^{-12}	8.5×10^{-12}
K_θ^i (radians)	0.36 (20.6°)	0.36 (20.6°)	0.36 (20.6°)

Figure 14 depicts the time histories of the component plume densities due to Alexandria, Cairo, and Damascus, as well as the total density due to all plume sources. With reference to this figure, one sees that the majority of the total plume density originates from Cairo. A comparison between the plume density computed using the model and that reconstructed using the E3 telemetry data is given in Fig. 15. In spite of the simplicity of the plume model used, there is a good comparison between $\rho_{\text{Reconstructed}}^{\text{E3}}(t)$ and $\rho_{\text{Model}}^{\text{E3}}(t)$. The mean value of the fitting error is 0.435×10^{-12} kg/m^3 which is only 7.5% of the peak value of the reconstructed density (5.96×10^{-12} kg/m^3).

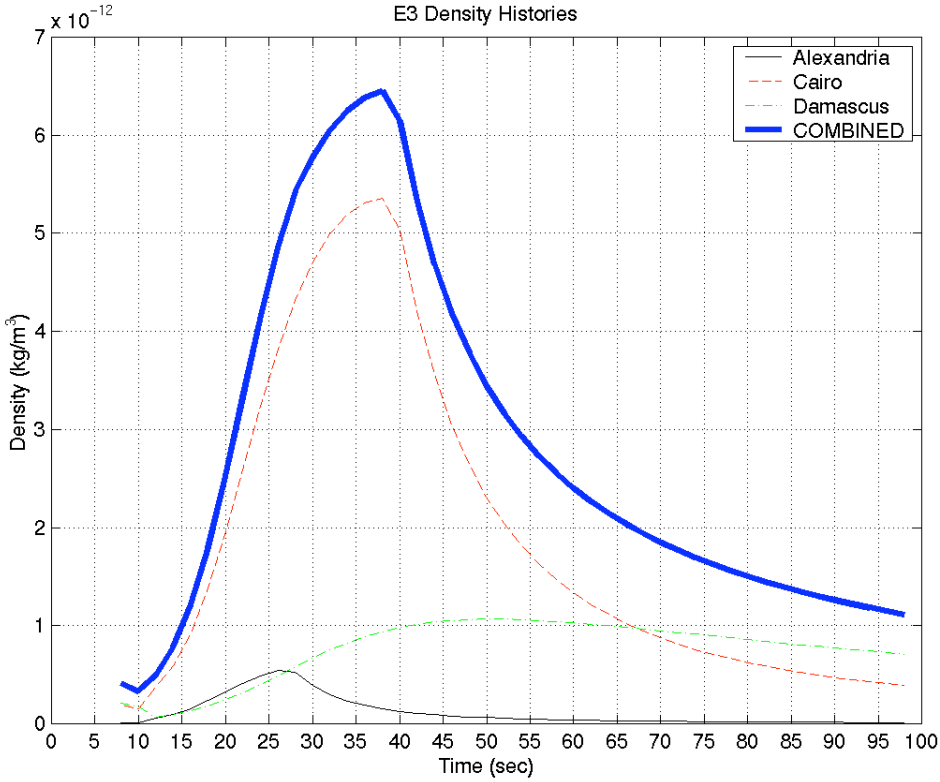

Fig. 14 Time Histories of Total and Component Enceladus Plume Density (for E3)

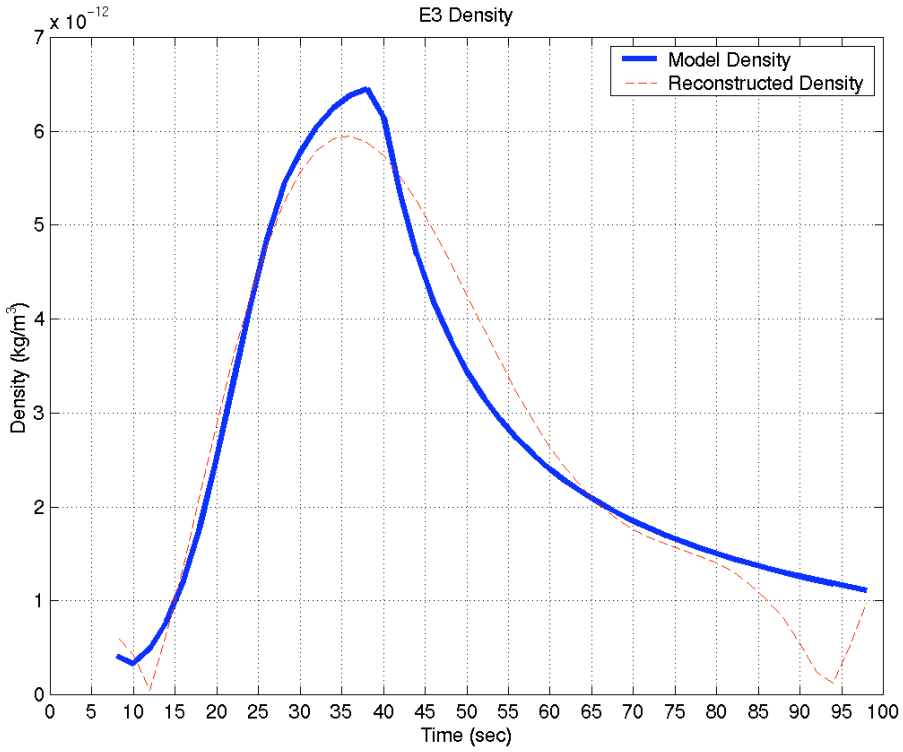

Fig. 15 Time Histories of Reconstructed and Modeled Enceladus Plume Density (for E3)

Measurements made by the Cassini INMS team on the density and structure of Enceladus' south polar plume during the E3 and E5 flybys are reported in Ref. 17. For the E3 flyby, the peak INMS-based plume density is 1.8×10^{-12} kg/m^3 which occurred at ECA+50 s when the Enceladus-relative altitude is 528 km. This INMS-based peak density differed by a factor of >3 from that reported here. See Table 4 for details. Moreover, the authors of Ref. 17 attributed the sharp H_2O signal measured at ECA+50 s to the Damascus plume jet. In contrast, our work concluded that most of the disturbance torque experienced by Cassini came from the Cairo plume jet. Future analyses of science and engineering data collected from other low-altitude Enceladus flybys (for example, Enceladus-9) will help to unlock the mystery behind the complex but interesting structure of the Enceladus plume.

Table 4
A Comparison of Peak Enceladus Plume Density As Estimated by INMS and AACS

Reconstructed by	Enceladus Flyby	ECA Altitude[++] [km]	Peak Density Occurred at time [s]	Altitude at which peak density occurred [km]	Peak Density [10^{-12} kg/m^3]
AACS	E3	47.9	ECA+34	322	5.6-5.96
AACS	E4	49.4	ECA+26	298	6.1[★]
AACS	E5	24.6	ECA+20	198	12.5[★]
INMS	E3	47.9	ECA+50	528	1.8±0.2[+]
INMS[★★]	E5	24.6	ECA+30	347	8.3±0.4[+]

[★]From unpublished data reconstructed by the Cassini AACS Mission Operations team.
[+]From Ref. 17.
[++]From Ref. 24.
[★★]INMS has no E4 data. The spacecraft attitude for the E4 flyby wasn't optimized for INMS.

IX. Conclusions

For Enceladus flybys on reaction wheels, one can use the unique and known transfer function between the disturbance torque and the attitude control error to estimate the plume torque on the spacecraft. The effectiveness of this methodology is established using telemetry data collected from the Enceladus-3 flyby in March 2008. Next, we modeled the plume density due to each jet as a function of both the radial and angular distances of the spacecraft from the plume center. For the limited-scope of our work, we retain only two free parameters for each plume model. We also assume that the total plume density experienced by the spacecraft could be approximated by the superposition of the component plume densities. By comparing the time history of the reconstructed E3 plume density with that predicted by the plume model, values of plume model parameters are determined. In spite of the simplicity of the plume model, the comparison between the reconstructed and the modeled densities is fairly good. The mean fitting error of 0.435×10^{-12} kg/m^3 is only 7.5% of the peak value of the reconstructed density. In comparing plume density estimated from this work with those derived using data collected by other Cassini science instruments, we found noticeable differences in plume density estimates that could not be explained by inaccuracies of the techniques involved. Future analyses of science and engineering

data collected from other Enceladus flybys will help to unlock the mystery behind the complex but interesting structure of the Enceladus plumes.

Acknowledgments

The work described in this paper was carried out by the Jet Propulsion Laboratory (JPL), California Institute of Technology, under contract with the National Aeronautics and Space Administration. Reference to any specific commercial product, process, or service by trade name, trademark, manufacturer, or otherwise, does not constitute or imply its endorsement by the United States Government or the Jet Propulsion Laboratory, California Institute of Technology. Laura Burke, Amanda Hendrix, Charles Kirby, Cliff Lee, and Fred Pelletier, our colleagues at JPL, had provided us with helpful supports. We are also indebted to following Cassini scientists for helpful discussions: Prof. Hunter Waite and Dr. Benjamin Teolis (both are affiliated with the Southwest Research Institute) and Prof. Krishan Khurana (who is affiliated with the University of California at Los Angeles). All errors of fact or interpretation are of course the responsibility of the authors.

References

[1]Porco, C.C., Helfenstein, P., Thomas, P.C., Ingersoll, A.P., Wisdom, J., West, R., Neukum, G., Denk, T., Wagner, R., Roatsch, T., Kieffer, S., Turtle, E., McEwen, A., Johnson, T.V., Rathbun, J., Veverka, J., Wilson, D., Perry, J., Spitale, J., Brahic, A., Burns, J.A., DelGenio, A.D., Dones, L., Murray, C.D., Squyres, S., "Cassini observes the active south pole of Enceladus," Science 311, 43-64 (2006).

[2]Hedman, M.M., Nicholson, P.D., Showalter, M.R., Brown, R.H., Buratti, B.J., and Clark, R.N., "Spectral Observations of the Enceladus Plume with Cassini-VIMS," The Astrophysical Journal, 693:1749-1762, 2009 March 10.

[3]Matson, D.L., Castillo, J.C., Lunine, J., and Johnson, T.V., "Enceladus' plume: Compositional evidence for a hot interior," Icarus 187 (2007) 567-573.

[4]Waite, H.J., et al, "Cassini Ion and Neutral Mass Spectrometer: Enceladus Plume Composition and Structure," Science 311, 1419 (2006).

[5]Hansen, C.C., Esposito, L., Stewart, I.F., Colwell, J., Hendrix, A., Pryor, W., Shemansky, D., and West, R., 2006, "Enceladus' Water Vapor Plume," Science 311, 1422.

[6]Hansen, C.C., Esposito, L., Stewart, I.F., Meinke, B., Wallis, B., Colwell, J., Hendrix, A.R., Larsen, K., Pryor, W., and Tian, F., "Enceladus' Water Vapor Jets Inside the Plume of Gas leaving Enceladus," Nature, Volume 456, No. 27, 477-479, November 2008.

[7]Spitale, J.N., and Porco, C.C., "Association of the jets of Enceladus with the warmest regions on its south-polar fractures," Nature 449, 695-697 (2007).

[8]Smith-Konter, B., and Pappalardo, R.T., "Tidally driven stress accumulation and shear failure of Enceladus's tiger stripes," Icarus 198, 435-451 (2008).

[9]Lee, A.Y., and Hanover, G., "Cassini Attitude Control System Flight Performance," AIAA Guidance, Navigation, and Control Conference and Exhibit, AIAA-2005-6269, San Francisco, CA, Aug. 15-18, 2005.

[10]Macala, G.A., "Design of the Reaction Wheel Attitude Control System for the Cassini Spacecraft," Paper AAS 02-121, AAS/AIAA Space Flight Mechanics Meeting, San Antonio, Texas, January 27-30, 2002.

[11]Rappaport, N.J., Iess, L., Tortora, P., Anabtawi, A., Asmar, S., Somenzi, L., and Zingoni, F., "Mass and Interior of Enceladus from Cassin Data Analysis," Icarus, 190(2007), 175-178.
[12]Feldman, A.W., Brown, J.M., Wang, E.K., Peer, S.G., and Lee, A.Y., "Reconstruction of Titan Atmosphere Density using Cassini Attitude Control Flight Data," 17th AAS/AIAA Space Flight Mechanics Meeting, AAS-07-187, Sedona, AZ, Jan. 28-Feb. 01, 2007.
[13]Sarani, S., "A Novel Methodology for Reconstruction of Titan Atmospheric Density Using Cassini Guidance, Navigation, and Control Data," Paper AIAA 2007-6343, Proceedings of the AIAA Guidance, Navigation, and Control Conference, August 20-23, Hilton Head, South Carolina, 2007.
[14]Brown, Jay, Wang, Eric, Hernandez, Juan, and Allan Y. Lee, "Importance of Model Simulations in Cassini In-flight Mission Events," Paper AIAA 2009-5762, Proceedings of the AIAA Guidance, Navigation, and Control Conference, August 10-13, Chicago, IL, 2009.
[15]Jaffe, L. and Herrell, L., "Cassini Huygens Science Instruments, Spacecraft, and Mission," Journal of Spacecraft and Rockets, Vol. 34, No. 4, 1997, pp. 509-521.
[16]Waite, J. H., et al., The Cassini Ion and Neutral Mass Spectrometer (INMS) Investigation, Space Sci. Rev., 114, 113, 2004.
[17]Teolis, B.D., Perry, M.E., Magee, B.A., Westlake, J., and Waite, J.H., "Detection and measurement of ice grains and gas distribution in the Enceladus plume by Cassini's Ion Neutral Mass Spectrometer" (this paper has been submitted to the Journal of Geophysical Research on December 14, 2009).
[18]Krishan Khurana, Michele K. Dougherty, Christopher T. Russell, and Jared S. Leisner, "Mass Loading of Saturn's Magnetosphere Near Enceladus," Journal of Geophysical Research, Vol. 112, A08203, 2007.
[19]Private communications between Prof. Krishan Khurana, UCLA, and the first author of this paper (Allan Y. Lee) on February 23-24, 2010.
[20]This image is copied from http://ciclops.org. Courtesy of University of Arizona, Jet Propulsion Laboratory (California Institute of Technology), and the National Aeronautics and Space Administration (NASA).
[21]Saur, J., N. Schilling, F. M. Neubauer, D. F. Strobel, S. Simon, M. K. Dougherty, and C. T. Russell (2008), Evidence for temporal variability of Enceladus' gas jets: Modeling of Cassini observations, Geophysical Research Letter, 35, L20105, doi:10.1029/2008GL035811.
[22]Nelder, J. A., and Mead, R. A., "Simplex Method for Function Minimization," *Computer Journal,* Vol. 7, No. 4, 1965, pp. 308-313.
[23]Lee, A.Y., "Optimal Autorotational Descent of a Helicopter with Control and State Inequality Constraints," AIAA Journal of Guidance, Control, and Dynamics, Vol. 13, No. 5, pp. 922-924, September-October 1990.
[24]Criddle, K.E., et al, "Cassini Orbit Determination: Challenges and Triumphs Presented by Close Flybys of Enceladus," Paper AAS 09-1017, Proceedings of the 32nd Annual AAS Rocky Mountain Guidance and Control Conference, January 30 to February 4, 2009, Breckenridge, Colorado.
[25]Boice, D.C., Soderblom, L.A., Britt, D.T., Brown, R.H., Sandel, B.R., Yelle, R.V., Buratti, B.J., Hicks, M.D., Nelson, R.M., Rayman, M.D., Oberst, J., and Thomas, N., "The Deep Space 1 Encounter with Comet 19p/Borrelly," Earth, Moon, and Planets, 89, pp. 301-324, 2002.
[26]Yeoh, S.K., Kizer, J.R., Goldstein, D.B., Varghese, P.L., and Trafton, L.M., "Modeling the Gas/Particle Plume of Enceladus," 41st Lunar and Planetary Science Conference, The Woodlands, Texas, March 1-5, 2010.

Appendix A

Telemetry Data of Enceladus-4 Flyby

The time of Enceladus Closest Approach (ECA) was 2008-224T21:06:19 SCET. The ECA altitude was 50 km with an Enceladus-relative flyby velocity of 17.7 km/s (28° S, 98° W). The Cassini spacecraft was under reaction wheel control throughout the entire flyby. The flyby trajectory relative to key plume sources is depicted in Fig. A1. Near the ECA, the spacecraft was only slewed about its Z-axis. The three per-axis body rates of the spacecraft were depicted in Fig. A2. Fig. A3 depicts the time histories of the per-axis attitude control errors.

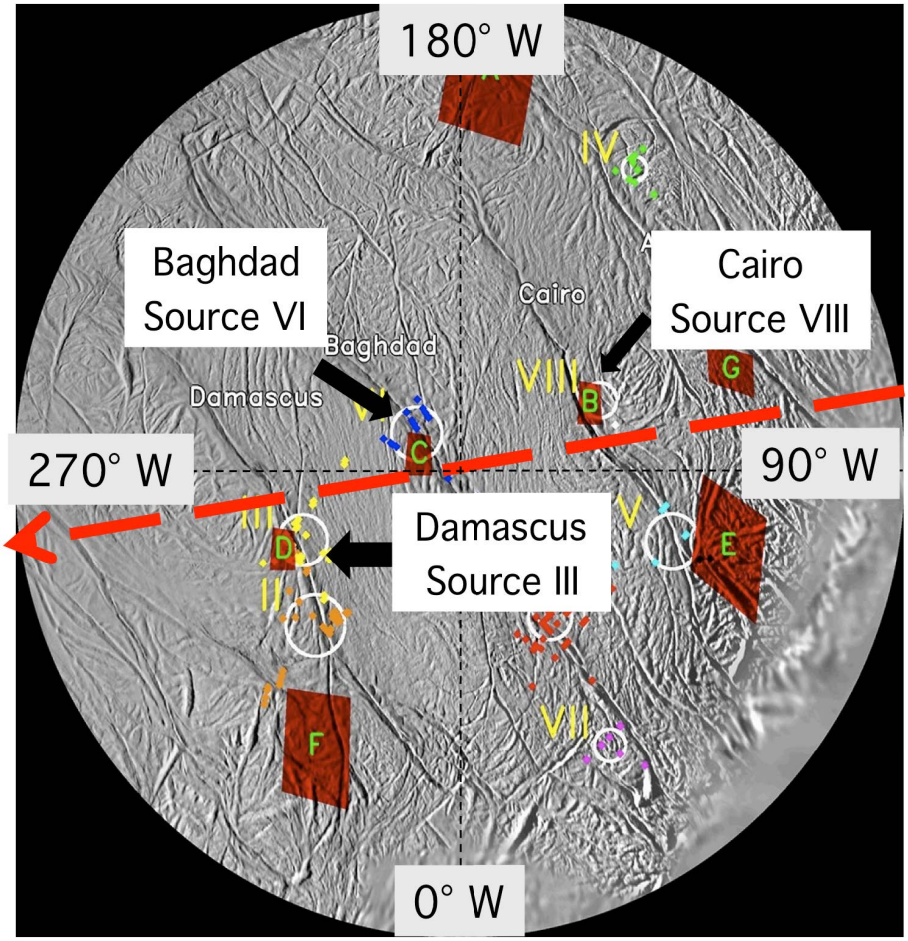

Fig. A1 Enceladus-4 Flyby Trajectory Projected on the Equatorial Plane of Enceladus (The flyby trajectory is depicted by the thick red arrow)

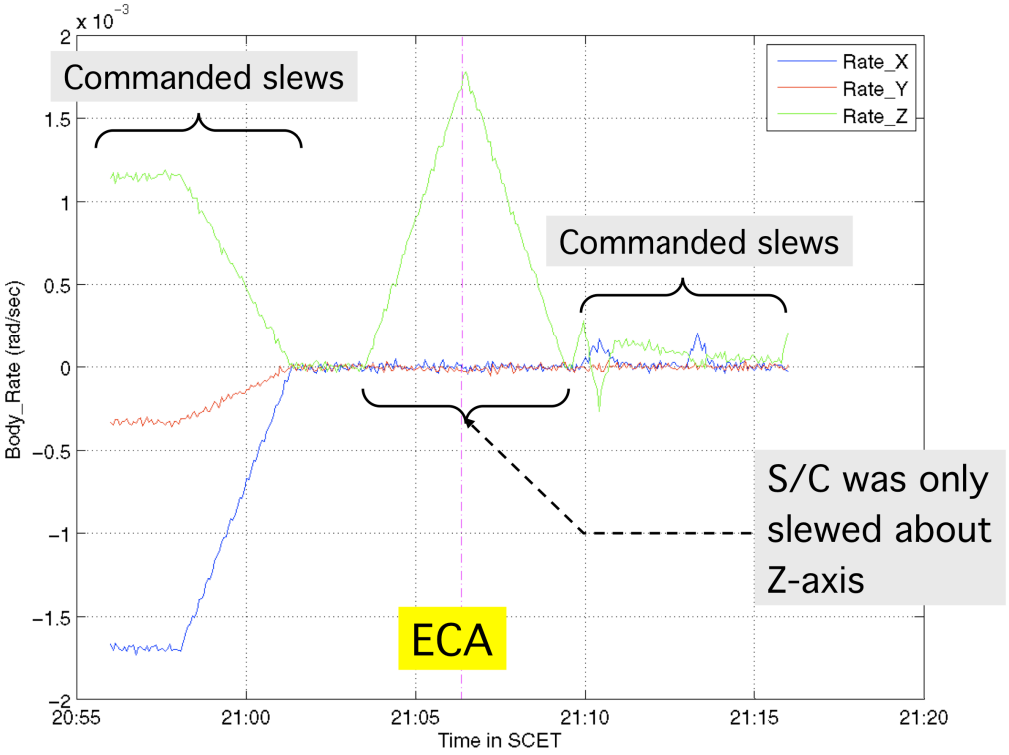

Fig. A2 Per-axis Spacecraft Body Rate Telemetry of the Enceladus-4 Flyby

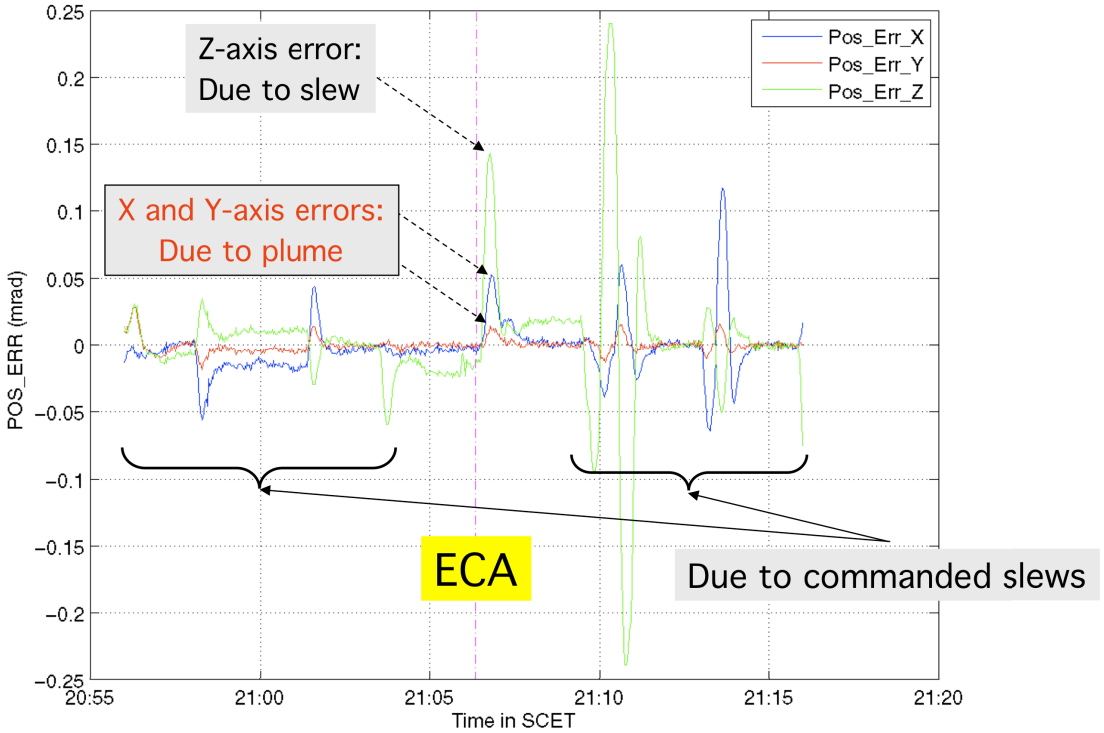

Fig. A3 Per-axis Attitude Control Error Telemetry of the Enceladus-4 Flyby

Appendix B

Geometry of Enceladus-3 Flyby

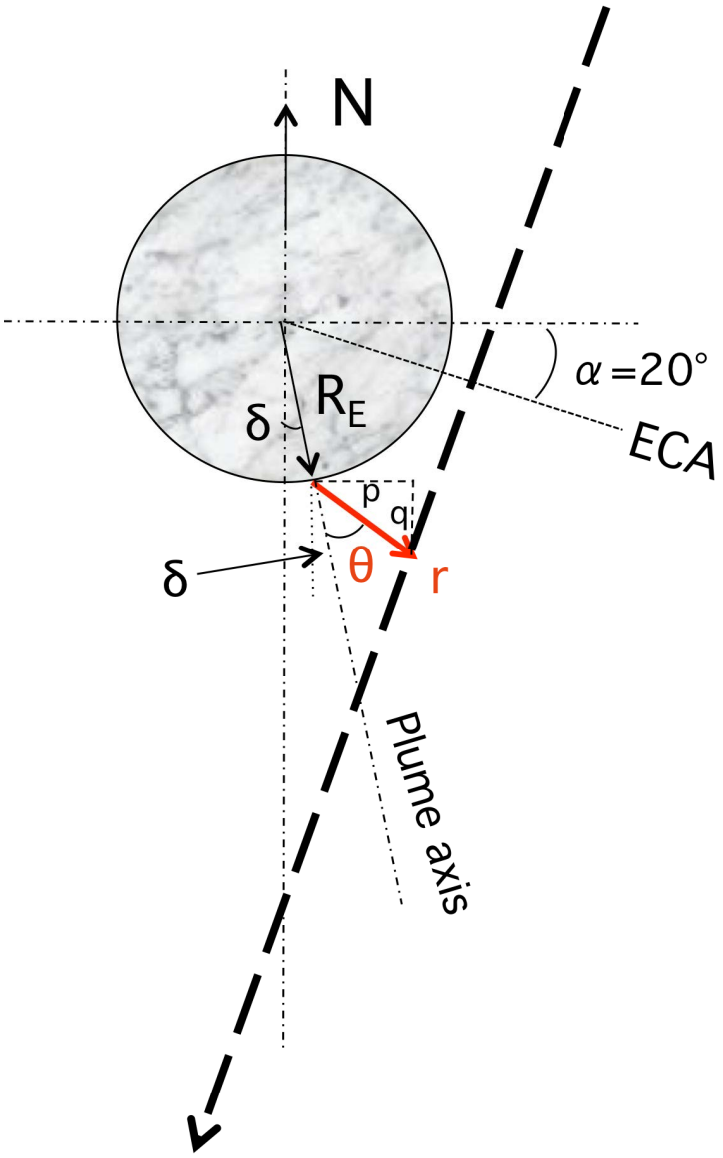

Fig. B1 Enceladus-3 flyby: Definitions of r, θ, and δ
(Note that δ is defined positive in the counter-clockwise direction)

Appendix C

Telemetry Data of Enceladus-9 Flyby (April 28, 2010)

The time of Enceladus Closest Approach (ECA) was 2010-118T00:10:17 SCET. The ECA altitude was 100 km with an Enceladus-relative flyby velocity of 6.51 km/s (89.29° S, 146.94° W). The Cassini spacecraft was under reaction wheel control throughout the entire flyby. The flyby trajectory relative to key plume sources is depicted in Fig. C1. Near the ECA of Enceladus-9 flyby, the spacecraft was quiescent about all axes. Figs. C2 and C3 depict the time histories of the three per-axis attitude control errors, and three per-axis attitude rate control errors, respectively.

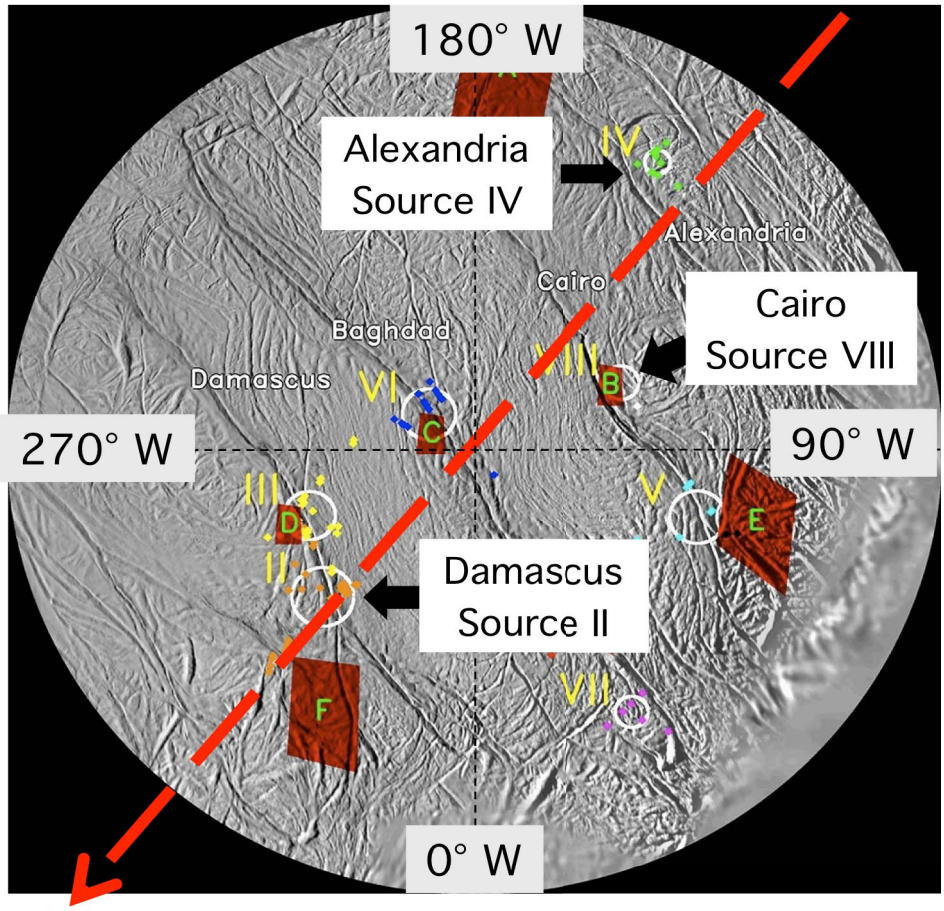

Fig. C1 Enceladus-9 Flyby Trajectory Projected on the Equatorial Plane of Enceladus (The flyby trajectory is depicted by the thick red arrow)

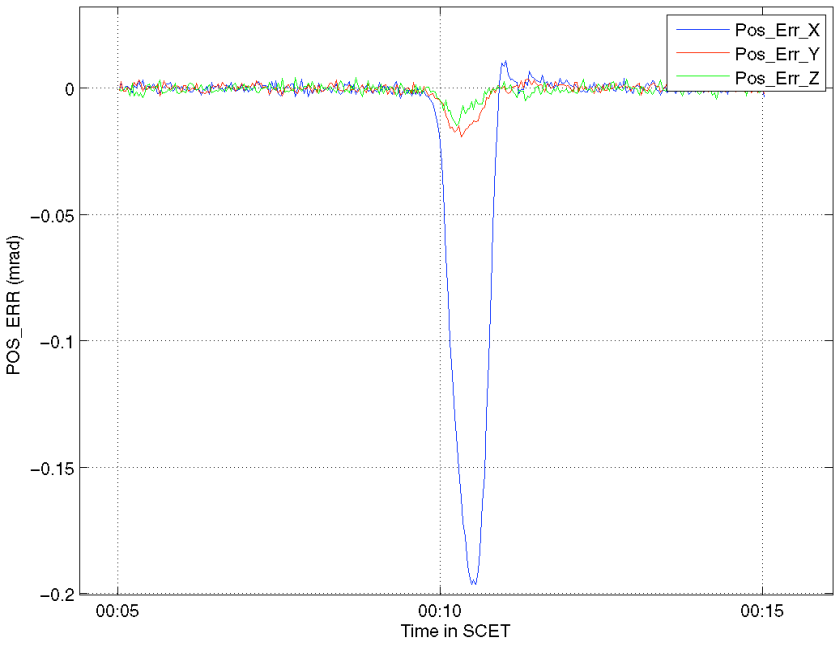

Fig. C2 Per-axis Attitude Control Error Telemetry of the Enceladus-9 Flyby (ECA was 00:10:17)

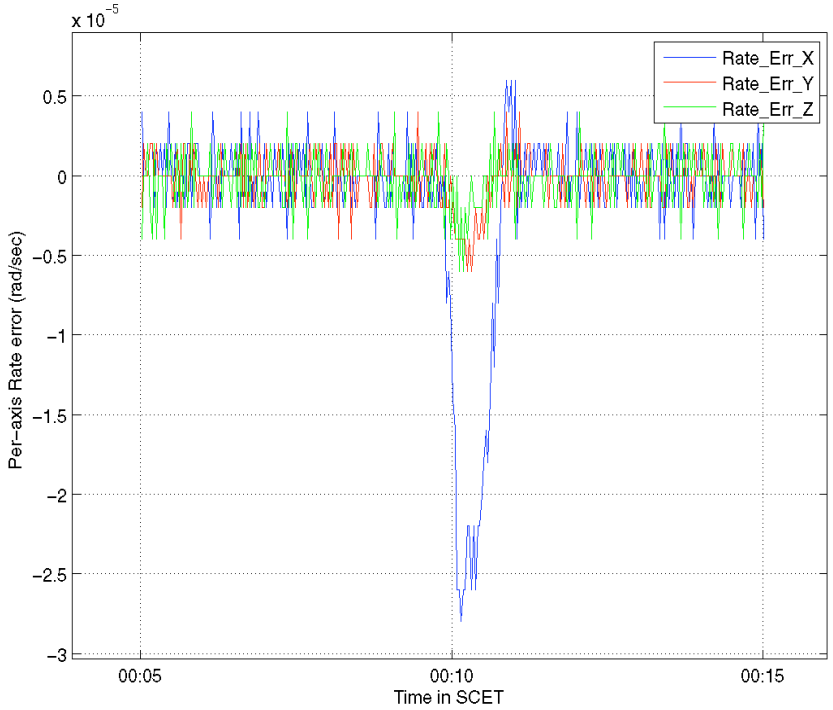

Fig. C3 Per-axis Attitude Rate Control Error Telemetry of the Enceladus-9 Flyby (ECA was 00:10:17)